JOURNAL OF GEOPHYSICAL RESEARCH, VOL. 113, D15S06, doi:10.1029/2007JD008665, 2008

Validation of Ozone Monitoring Instrument level 1b data products

M. Dobber,[1] Q. Kleipool,[1] R. Dirksen,[1] P. Levelt,[1] G. Jaross,[2] S. Taylor,[2] T. Kelly,[2] L. Flynn,[3] G. Leppelmeier,[4] and N. Rozemeijer[1,5]

Received 16 March 2007; revised 12 November 2007; accepted 14 December 2007; published 25 April 2008.

[1] The validation of the collection 2 level 1b radiance and irradiance data measured with the Ozone Monitoring Instrument (OMI) on NASA's Earth Observing System (EOS) Aura satellite is investigated and described. A number of improvements from collection 2 data to collection 3 data are identified and presented. It is shown that with these improvements in the calibration and in the data processing the accuracy of the geophysically calibrated level 1b radiance and irradiance is improved in the collection 3 data. It is shown that the OMI level 1b irradiance product can be reproduced from a high-resolution solar reference spectrum convolved with the OMI spectral slit functions within 3% for the Fraunhofer structure and within 0.5% for the offset. The agreement of the OMI level 1b irradiance data product with other available literature irradiance spectra is within 4%. The viewing angle dependence of the irradiance and the irradiance goniometry are discussed, and improvements in the collection 3 data are described. The in-orbit radiometric degradation since launch is shown to be smaller than 0.5% above 310 nm and increases to about 1.2% at 270 nm. It is shown how the viewing angle dependence of the radiance is improved in the collection 3 data. The calculation of the surface albedo from OMI measurement data is discussed, and first results are presented. The OMI surface albedo values are compared to literature values from the Total Ozone Mapping Spectrometer (TOMS) and the Global Ozone Monitoring Experiment (GOME). Finally, improvements in the spectral and spatial stray light corrections from collection 2 data to collection 3 data are presented and discussed.

Citation: Dobber, M., Q. Kleipool, R. Dirksen, P. Levelt, G. Jaross, S. Taylor, T. Kelly, L. Flynn, G. Leppelmeier, and N. Rozemeijer (2008), Validation of Ozone Monitoring Instrument level 1b data products, *J. Geophys. Res.*, *113*, D15S06, doi:10.1029/2007JD008665.

1. Introduction

[2] The Ozone Monitoring Instrument (OMI) was launched on 15 July 2004 on NASA's EOS-Aura satellite. The primary objective of the OMI instrument is to obtain daily global measurements of ozone and nitrogen dioxide in both the troposphere and stratosphere. The central science issues addressed by the OMI mission are the recovery of the ozone layer, the depletion of ozone at the poles, tropospheric pollution and climate change [*Levelt et al.*, 2006].

[3] The OMI instrument is a nadir-viewing ultraviolet-visible imaging spectrograph that uses two-dimensional Charge Coupled Device (CCD) detectors to register both the spectrum and the viewing angle perpendicular to the flight direction with a 115° wide swath, which enables global daily ground coverage with high spatial resolution. In this way tropospheric trace gases can be observed with high spatial resolution and cloud-free ground pixels are more easily obtained as compared to predecessor sensors. The instrument has three optical channels: UV1 (264–311 nm), UV2 (307–383 nm) and VIS (349–504 nm). The UV1/UV2 channel overlap covers 307–311 nm and the UV2/VIS channel overlap covers the wavelength range 349–383 nm. OMI delivers absolutely calibrated spectral radiance and irradiance level 1b data products in the spectral range 264–504 nm. A full description of the instrument and the on-ground calibration can be found in an earlier publication [*Dobber et al.*, 2006].

[4] The software that is used to process raw instrument data (level 0 data) to calibrated measurement data (level 1b data) is referred to as the Ground Data Processing Software (GDPS). The GDPS has been developed by Dutch Space in The Netherlands. The scientific responsibility for the OMI mission resides at the Royal Netherlands Meteorological Institute (KNMI). Data processing and operational aspects have been described in detail in an earlier publication [*van den Oord et al.*, 2006].

[5] The GDPS ingests level 0 data from the instrument, attitude and ephemeris data for the spacecraft and ancillary data (like near real-time ice and snow extent maps). Another important input file for the GDPS is the so-called Operational Parameter File (OPF), that contains all instrument

[1]Royal Netherlands Meteorological Institute, De Bilt, Netherlands.
[2]Science Systems and Applications Inc., Greenbelt, Maryland, USA.
[3]NOAA, Camp Springs, Maryland, USA.
[4]G & S Associates, Espoo, Finland.
[5]Also at TriOpSys b.v., Utrecht, Netherlands.

0148-0227/08/2007JD008665$09.00

calibration parameters needed for processing. This file is compiled from the on-ground and in-flight calibration databases. The latter is in turn compiled from the information in the level 1b data products. In this way it is possible to maintain the calibration accuracy in flight.

[6] The purpose of the present paper is to present validation results for the level 1b radiance and irradiance data products in the collection 2 data to identify improvements that are made to the GDPS and the OPF in the collection 3 data set, that will be publicly released. These improvements are described in detail in the remaining sections of this paper. All existing in-flight measurement data have been reprocessed using new versions of the GDPS (version 1.0.0) and the OPF to produce the collection 3 data. The following improvements have been identified from collection 2 data to collection 3 data: (1) higher frequency of CCD background corrections; (2) improved correction algorithm and parameters of spectral stray light in GDPS and OPF; (3) improved parameters for the irradiance goniometry correction in the OPF; (4) improved radiance radiometric calibration data for all viewing angles in the OPF; and (5) improved irradiance radiometric calibration data for all equivalent viewing angles in the OPF.

[7] These topics are discussed in detail in the sections below. In cases where we show and discuss the validation of the improved level 1b collection 3 data this is explicitly mentioned.

[8] The level 1b to level 2 retrieval algorithms use the ratio of the level 1b Earth radiance and the solar irradiance, called the Earth reflectance, as input. In this ratio many calibration inaccuracies that apply equally to both the radiance and irradiance cancel. This implies that the accuracy of the Earth reflectance is higher than that of the Earth radiance. Furthermore, most of the collection 2 level 2 data products have been produced using a fixed solar irradiance spectrum rather than a solar irradiance that is updated with the daily measurement frequency. In that case the Earth radiance has been corrected for the Earth–Sun distance. By using a fixed solar irradiance spectrum a number of calibration inaccuracies, for example the irradiance goniometry and inaccuracies originating from imperfect background correction in the irradiance, are avoided in the level 2 data products.

[9] The improvement from using daily measured background data to determine the dark current for the CCD images as compared to background data that are updated on a monthly basis or less is not discussed in detail here. This issue is related to in-flight radiation damage to both CCD detectors from high-energetic protons (>10 MeV) trapped in the Earth's magnetic field. This effect has been described and discussed in detail elsewhere [*Dobber et al.*, 2006].

2. Solar Irradiance Level 1b Data Product Validation

2.1. Central Viewing Direction Absolute Irradiance

[10] Understanding the in-orbit instrument throughput degradation is an important part of the in-flight calibration. Degradation can occur in instrument components that are used only in the radiance mode (the primary telescope mirror), in components that are used only in the irradiance mode (the solar mesh, diffuser and folding mirror) or in components that are common to both modes. Depending on which components are potentially degrading, the Earth reflectivity, the ratio of radiance and irradiance, may also be affected. For this reason it is important to identify the components that may be causing degradation.

[11] In the literature various solar reference spectra with high spectral resolution (better than 0.03 nm) and good spectral calibration (better than 0.002 nm), but with poor radiometric accuracy are available in the wavelength range 250–550 nm, for example [*Chance and Spurr*, 1997; *Hall and Anderson*, 1991; *Kurucz et al.*, 1984]. Various solar reference spectra with lower spectral resolution and good to excellent radiometric calibration (3–4%) in the same wavelength range are also available, for example [*Thuillier et al.*, 2003, 2004; *Floyd et al.*, 2003; *Gurlit et al.*, 2005]. For the latter spectra the instrument spectral slit functions are usually not known sufficiently accurate, which makes it difficult to compare these reference spectra radiometrically on their original measurement spectral resolution. In that case the spectral resolution is lowered by convolving the spectra with a known, spectrally broader, spectral slit function, for example a triangular or Gaussian slit function. In addition, the lower-resolution solar reference spectra have a much poorer spectral calibration accuracy than the high-resolution spectra. Thus, a high-resolution solar reference spectrum with good spectral calibration and sampling and good radiometric calibration is not readily available. We have derived such a high-resolution spectrum in the following way [*Dobber et al.*, 2008]: (1) Convolve the selected high-resolution spectrum with lower radiometric calibration accuracy from the literature with the optimized instrument spectral slit function for the selected lower-resolution solar reference spectrum with good radiometric calibration accuracy. (2) Interpolate the thus obtained high spectral sampling, low-resolution spectrum on the wavelength grid of the lower-resolution reference spectrum. (3) Divide the spectrum from the second step by the selected lower-resolution spectrum to obtain the fraction by which to multiply the selected original high-resolution spectrum used in the first step. (4) Interpolate the fraction from the third step to the high-resolution wavelength grid. (5) Multiply the original high-resolution spectrum with the radiometric correction factor from the fourth step.

[12] In this process the high-resolution and lower-resolution spectra from the literature need to be selected carefully. For the high-resolution spectrum the same approach as *Chance and Spurr* [1997] is followed to combine the UV spectrum of *Hall and Anderson* [1991], that covers the wavelength region between 200 and 310 nm and the ground-based high-resolution spectrum obtained at Kitt Peak [*Kurucz et al.*, 1984]. The final spectral calibration accuracy of this combined high-resolution spectrum is better than 0.001 nm above 305 nm and better than 0.002 nm below 300 nm. For the lower-resolution spectra from the literature the 0.15 nm resolution SUSIM data set from UARS [*Floyd et al.*, 2003] is used for the spectral region up to 410 nm and for the visible spectral region above 400 nm the balloon spectrum obtained for the SCIAMACHY validation [*Gurlit et al.*, 2005] is used. Further important details for the lower-resolution spectra such as the choice of the instrument spectral slit function and the improvement of the spectral calibration to better than 0.01 nm by compar-

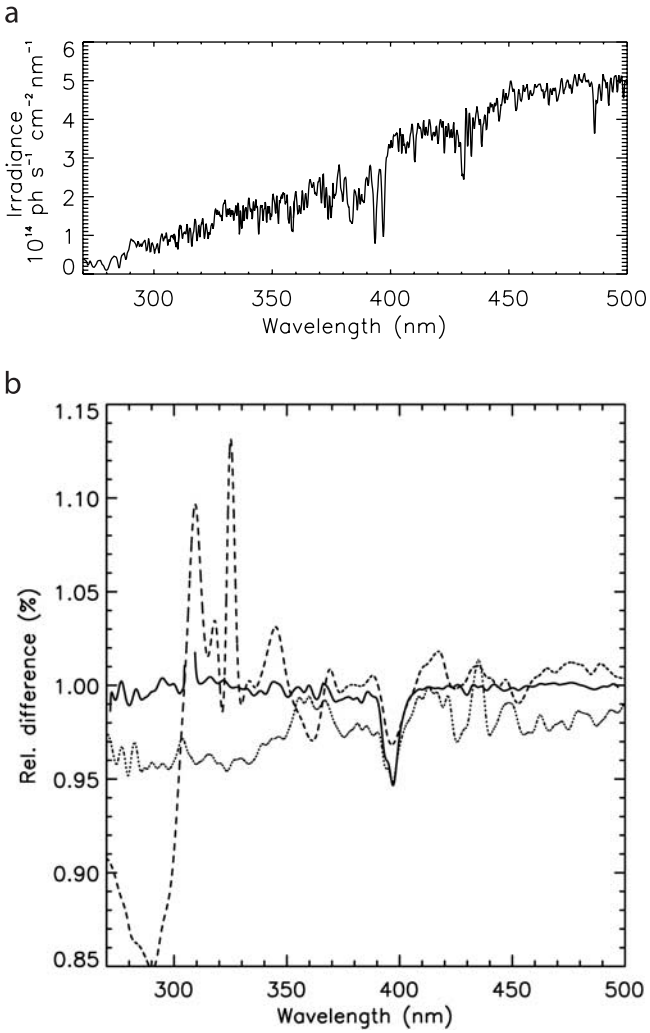

Figure 1. (a) OMI irradiance spectrum from orbit 2465 (31 December 2004) from the collection 3 data. (b) Comparisons at 2 nm resolution between the newly derived high-resolution solar reference spectrum [*Dobber et al.*, 2008] and the high-resolution spectrum of *Chance and Spurr* [1997] (dashed), the lower-resolution spectrum of *Thuillier et al.* [2003, 2004] (dotted) and the OMI irradiance measurement from orbit 2465 from the collection 3 data (solid line).

ison to the high-resolution spectrum also need to be taken into account [*Dobber et al.*, 2008]. The result is a high-resolution solar reference spectrum (0.025 nm) in the 250–550 nm spectral range with a spectral sampling of 0.01 nm, a spectral calibration accuracy better than 0.001 nm above 305 nm and better than 0.002 below 300 nm and a good radiometric calibration that can be traced to available literature solar irradiance reference spectra.

[13] In Figure 1 the newly derived high-resolution spectrum is compared to lower- and higher-resolution solar reference spectra from the literature by first convolving all spectra to the same spectral resolution using the same slit function with a resolution of about 2 nm and subsequently calculating the ratio of two spectra. A 2 nm resolution has been used for this comparison in order to focus on the overall radiometric calibration rather than the differences in Fraunhofer structure. The comparison with the *Chance and Spurr* [1997] spectrum shows large differences below 310 nm. This was expected from the fact that the Chance and Spurr spectrum was not optimized radiometrically for that wavelength range.

[14] The agreement between the convolved high-resolution spectrum and the lower-resolution irradiance spectrum from *Thuillier et al.* [2004] is within about 2% for higher-frequency structures (Fraunhofer lines, with the exception of the time-variable CaII HK lines between 390 and 400 nm), within about 3% for lower-frequency structures, tentatively attributed to radiometric calibration errors in both spectra under consideration, and within about 2% (at 500 nm) to 4% (at 270 nm) for the difference over the whole 270–500 nm wavelength range. The latter is in agreement with the observation made by *Thuillier et al.* [2004] that the SUSIM irradiance is 3–4% lower than the SOLSPEC irradiance [*Thuillier et al.*, 2003]. The conclusion is that the newly derived high-resolution irradiance spectrum agrees within 4% with existing solar reference irradiance spectra from the literature.

[15] OMI measures the Sun over an onboard reflection diffuser that illuminates the complete entrance slit of the spectrometer. As a result all CCD rows in the irradiance mode equivalent to the viewing angles in the radiance mode perpendicular to the satellite velocity vector are simultaneously illuminated in the irradiance mode. In this paper we use viewing angle and row interchangeably, because they both indicate the same dependencies [*Dobber et al.*, 2006]. The OMI optical design ensures that for each viewing angle the illumination of the spectrometer's entrance slit is exactly the same for the Earth radiance and Sun irradiance modes. For this reason the spectral slit functions are the same for Earth radiance and Sun irradiance, which was verified experimentally on the ground.

[16] For OMI the newly derived high-resolution spectrum with high spectral sampling is convolved with the accurately known OMI spectral slit functions [*Dirksen et al.*, 2006], interpolated onto the spectral grid of the OMI irradiance measurement and compared on the OMI spectral resolution (0.63 nm in UV1 and VIS, 0.42 nm in UV2) to the OMI irradiance measurement. Differences are examined on high spectral frequency (Fraunhofer lines) and on low spectral frequency level (radiometric calibration differences). The result is shown in Figure 2 for the nadir viewing direction for the level 1b irradiance spectrum of 31 December 2004 (orbit 2465, collection 3 data). For this day the azimuth angle is nominal (25.75°), which implies that potential additional errors originating from the irradiance goniometry correction (see section 2.3) are minimized. For the improvement from collection 2 to 3 we used the modified stray light correction (see section 6) and the newly derived high-resolution solar reference spectrum discussed above to optimize the OMI absolute irradiance calibration in the OPF using only spectrally broad radiometric correction factors. For this reason it is not surprising that the result as shown in Figure 2 is close to one. The maximum deviation from unity is generally below ±0.5% and the fine structure, mainly correlated to solar Fraunhofer lines, is within ±3%, with the exception of the two strong time-variable CaII HK Fraunhofer lines between 390 and 400 nm.

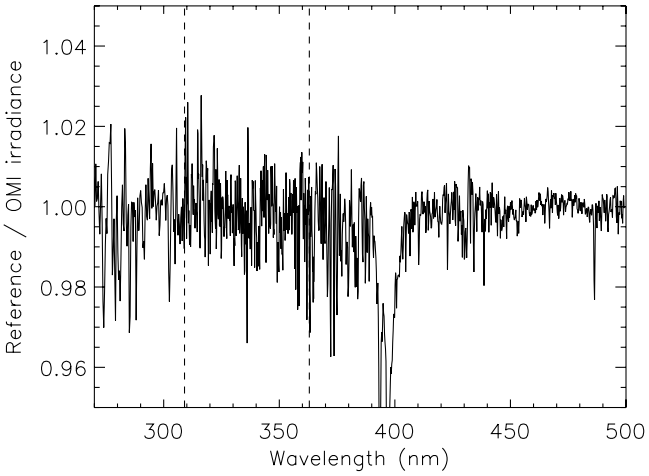

Figure 2. Ratio of the newly derived high-resolution solar reference spectrum [*Dobber et al.*, 2008] convolved with the measured OMI spectral slit functions and the measured OMI level 1b irradiance from orbit 2465 (31 December 2004) from the collection 3 data. The vertical dashed lines indicate the OMI channel boundaries between UV1 and UV2 at 309 nm and between UV2 and VIS at 363 nm.

Figure 1 also shows the same OMI plot as Figure 2, but on the same 2 nm resolution as the other plots in Figure 1. Figure 1a shows the OMI level 1b irradiance spectrum of orbit 2465 from collection 3 data for reference.

[17] The OMI level 1b absolute irradiance for the nadir viewing direction, with an estimated absolute accuracy of about 5% [*Dobber et al.*, 2006], agrees with the newly derived high-resolution solar reference spectrum (Figure 2), with the lower-resolution irradiance spectra from SUSIM [*Floyd et al.*, 2003] and from the balloon measurements of *Gurlit et al.* [2005], and with the lower-resolution irradiance spectrum from *Thuillier et al.* [2004] to within 4% over the wavelength range 270–500 nm.

2.2. Irradiance Viewing Angle Dependence

[18] The OMI level 1b irradiance data product depends on wavelength (column number) and on row number on the CCD detectors (equivalent to viewing angle in the radiance mode), but also on the incident azimuth and elevation angles of the Sun on the reflection diffuser. Figure 3a shows the viewing angle dependence of the OMI level 1b irradiance spectrum for orbit 2465 of 31 December 2004 for the collection 2 data for the VIS channel. The depicted behavior is representative also for other orbits and channels. The response for all viewing angles is shown relatively to the nadir viewing direction, which is therefore equal to one by definition. Since the solar spectrum is the same, irrespective of the viewing angle, the relative responses shown in Figure 3 should be equal to one for all rows and columns. This is not the case for collection 2 data: there is a row (viewing angle) dependence, that is mostly column (wavelength) independent. The observed dependence is caused by calibration inaccuracies originating from specular reflections between the onboard diffuser and the backside of the solar mesh [*Dobber et al.*, 2006]. By adjusting the instrument irradiance radiometric calibration in the OPF based on the observed dependence of about 2% in the collection 2 data the viewing angle dependence was improved for the collection 3 data to a row-dependent irradiance measurement precision of about 0.4% for UV1 and 0.2% for UV2 and VIS, leading to the results shown in Figure 3b. The improvement from collection 2 to collection 3 data as shown in Figure 3 is representative also for the UV1 and UV2 channels.

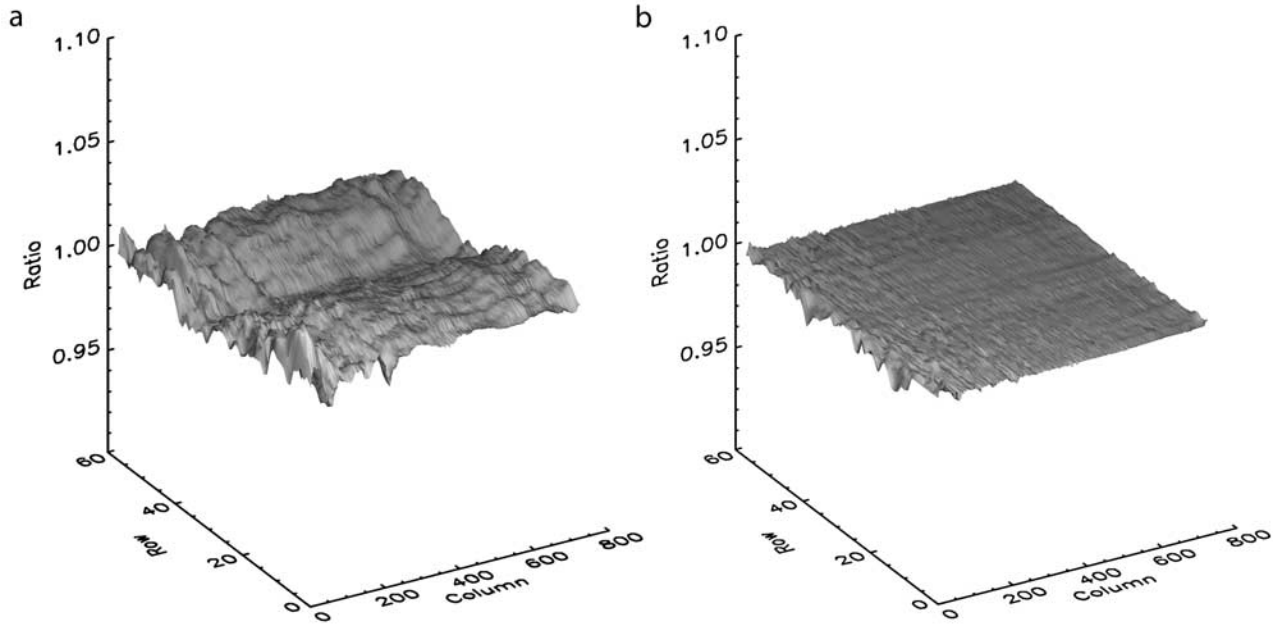

Figure 3. (a) Irradiance viewing angle dependence relative to nadir in the VIS channel for orbit 2465 (31 December 2004) for collection 2 data. (b) Irradiance viewing angle dependence relative to nadir in the VIS channel for orbit 2465 (31 December 2004) for collection 3 data.

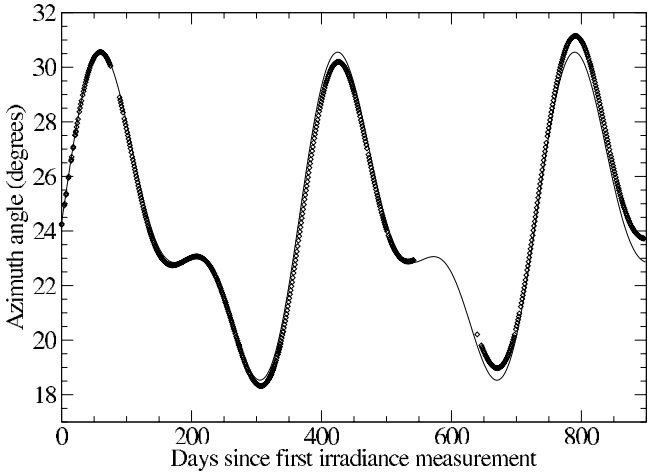

Figure 4. Azimuth angle as a function of days since the first irradiance measurement in September 2004. The diamonds are the actual measurement points, and the fitted solid line is included to guide the eye.

2.3. Irradiance Goniometry

[19] As described above the OMI irradiance also depends on azimuth and elevation angle of the Sun on the onboard reflection diffuser. The elevation angle is the angle that changes with orbit position, whereas the azimuth angle changes with season. In orbit the elevation angle ranges from −4.0 to +4.0° and the azimuth angle ranges from about 18 to 31°. The irradiance goniometry itself depends on detector column (wavelength) and on detector row (viewing angle) as well.

[20] The OPF calibration parameters for the irradiance goniometry were originally derived from on-ground measurement data that suffered from limited sampling in the azimuth and elevation dimensions as well as from poor signal-to-noise. For this reason an update using in-flight measurement data was necessary. This update was derived by attributing changes in the sensor irradiance response over the course of the first year after launch to goniometry variations. This assumption is reasonable, because the observed radiometric degradation in the irradiance mode in the first year in orbit is less than 0.3% for all wavelengths (see section 3), whereas the irradiance goniometry inaccuracies were at least an order of magnitude larger than that. The accuracy of the irradiance goniometry improved significantly to residues smaller than 0.5% for UV1 and smaller than 0.2–0.3% for UV2 and VIS by using the in-flight measurement data instead of the on-ground measurement data as a result of higher sampling in the angle dimensions and much better signal-to-noise.

[21] Figure 4 shows the azimuth angle as encountered by OMI in orbit for 2.5 years of measurement data. It can be observed that besides the expected seasonal dependence there is a drift in the azimuth angle as a function of time: When looking at the maximum azimuth angles there is an increase of about 0.5° over about 2 years. The reason for this is the drift in the ascending node crossing time of the orbit plane. This time is approximately 1342 local time (LT), but it is operationally allowed to drift between 1340 and 1400 LT. The drift resulted in the fact that in October–November 2006 azimuth angles of larger than 31.0° were observed by OMI for the first time in orbit. Since the OPF coefficients were derived from the first year of in-flight data (maximum azimuth angle smaller than 31.0°) this resulted in extrapolation in the irradiance goniometry correction algorithm, which in turn resulted in radiometric deviations of larger than 5% for azimuth angles larger than 31.0° for the UV1, UV2 and VIS channels for the onboard quartz volume Sun diffuser. The radiometric deviations are defined as the ratios of the calibrated level 1b irradiance data products at various azimuth angles divided by the calibrated level 1b irradiance data product for the nominal azimuth angle of 25.75°. These deviations show how well the irradiance goniometry calibration parameters from the OPF can reproduce the actually measured response and correct for it.

[22] New irradiance goniometry OPF parameters have been derived using all available 2.5 years of in-flight measurement data by fitting the elevation and azimuth angle, row and wavelength dependencies. This improved the accuracy of the irradiance goniometry correction for the larger azimuth angles in the collection 3 data for the quartz volume diffuser to about 0.5% for UV1 and 0.2–0.3% for UV2 and VIS, except in UV2 for row numbers smaller than 15 and for azimuth angles larger than 31.0°, where deviations of up to 1% occur. When the azimuth angle on the diffuser falls below 18.3° or exceeds the value of 31.2° in the future, similar calibration inaccuracies as described above may be anticipated.

3. Irradiance Radiometric Degradation

[23] The in-orbit radiometric stability of the OMI instrument since launch has been investigated using the Sun measurement data and the internal white light source (WLS) measurement data. Figure 5 shows the Sun measurements over the onboard quartz volume diffuser from launch to launch+2.5 years. In this plot detector areas

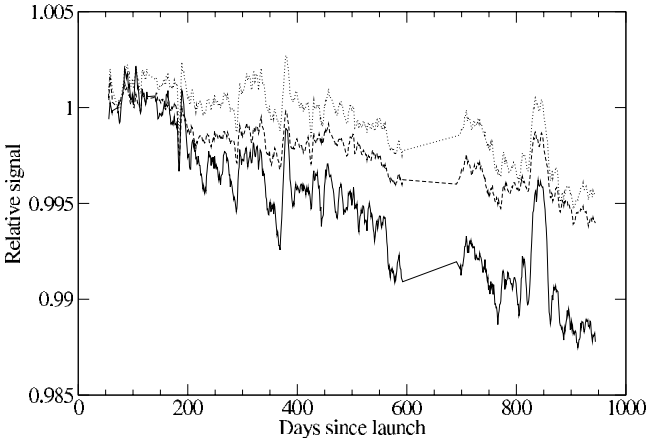

Figure 5. OMI in-orbit radiometric stability as observed with the Sun over the onboard quartz volume diffuser for the UV1 channel (solid line, bottom curve), the UV2 channel (dotted line, top curve) and the VIS channel (dashed line, middle curve) from launch to launch plus 2.5 years.

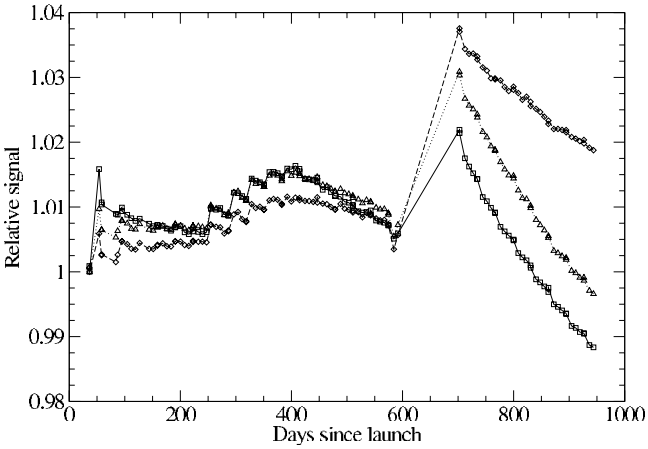

Figure 6. OMI in-orbit radiometric stability as observed with the internal WLS for the UV1 channel (solid line and squares), the UV2 channel (dotted line and triangles) and the VIS channel (dashed line and diamonds) from launch to launch plus 2.5 years.

have been averaged per channel, so the wavelength resolution within each optical channel is lost. For the time period 27 February to 16 June 2006 no Sun measurements are available. It can be observed that the optical throughput degradation of the irradiance mode is about 1.2% for UV1 and 0.5% for UV2 and VIS after 2.5 years in orbit. The observed variations at, e.g., day 850 originate from inaccuracies in the irradiance goniometry calibration (see section 2.3). The observed in-orbit degradation is low for a spectrometer such as OMI, that measures in the ultraviolet-visible wavelength range.

[24] Figure 6 shows a similar plot as Figure 5, but now for the WLS. The same data gap as for the Sun measurements exists also for the WLS measurements. After this data gap the WLS response is significantly higher than before the gap, even higher than immediately after launch. This effect, which is not understood, is attributed to the WLS itself, because the change is not observed in the Sun measurements (see Figure 5). Variation in the WLS response data in the order of about 3% can be observed, which can also be mostly attributed to the long-term stability of the lamp itself rather than the OMI radiometric stability, again because this behavior is not observed for the Sun measurement data (Figure 5). The lamp was not originally designed to provide long-term high radiometric accuracy or stability. There seems to be no consistent trend upward or downward in the WLS data. If a degradation trend is to be derived from Figure 6 for the WLS it is certainly not larger than 2% for all channels.

[25] Figure 5 shows the in-orbit optical throughput degradation in time for the irradiance measurements. The optical light path for the Sun measurements is via a solar mesh, the diffuser and a folding mirror to the rest of the optics. The Earth radiance observation mode uses the primary telescope mirror, that is not used in the WLS or Sun modes, instead of the solar mesh, diffuser and folding mirror. This primary telescope mirror may be subject to optical degradation, which necessarily has to be examined using the radiance data. This is more complicated, since the radiance light is much more variable than the WLS or sunlight. The degradation observed in the Earth radiance light path is discussed in another paper in this issue [*Jaross and Warner*, 2008]. Jaross shows that no long-term in-orbit degradation is observed in the radiance mode at 360 nm from launch until launch+3 years with an accuracy of about 1%. This suggests that the degradation of the primary telescope mirror at 360 nm for this time period is below 1%. The observed degradation in UV2 in the irradiance mode amounts to about 0.5%, which is lower than the precision with which the degradation of the radiance mode at this wavelength can be established. As a result of the fact that the in-orbit degradation observed thus far in both the radiance and irradiance modes is low, it is not possible to establish with absolute certainty which optical components cause the observed small degradation.

[26] The observed degradation in the Sun measurement mode will be further investigated in the future by comparing the daily Sun measurements over the quartz volume diffuser with the Sun measurements over the two aluminum diffusers, that are measured once per week and once per month.

4. Radiance Viewing Angle Dependence

[27] The viewing angle dependence of the level 1b radiance measurement data has been investigated by looking at the Earth radiances over snow/ice and land surfaces, and comparing these with calculated theoretical predictions. The illumination and viewing geometry of the data are carefully chosen to minimize the sensitivity to the non-Lambertian reflective characteristics of these surfaces. The viewing angle dependence is calculated as the response at all viewing angles divided by the response at the nadir viewing angle. If the calibration of the viewing angle dependence would be perfect this ratio should be equal to one for all viewing angles when normalized with respect to the nadir viewing direction. Since the comparisons are made to Sun-normalized radiances, the results presented here do not include errors common to both radiance and irradiance measurements. However, Figure 3 suggests that these errors are relatively small.

[28] The evaluation of the measured radiances over Antarctica utilize a surface reflectivity model to account for non-Lambertian effects and a radiative transfer model to predict results at the atmosphere [*Jaross and Warner*, 2008]. The investigation of the viewing angle dependence of the radiance over cloud-free, verdant land scenes uses a similar radiative transfer model, but no correction for non-Lambertian reflectivity. Because the reflectivity of such land surfaces is uniformly low in the UV ($\leq$2%), the angular dependence of these radiances is dominated by Rayleigh scattering in the atmosphere. Only scenes with low aerosol contamination were considered in our analysis. Aerosols are screened using the ratio of measured reflectances at 331 nm and 360 nm compared to the expected ratios for a pure Rayleigh-scattering atmosphere.

[29] We believe that the swath dependence uncertainty, the ability to validate sensor response at far off-nadir view angles relative to the response at nadir, is within 2% for both

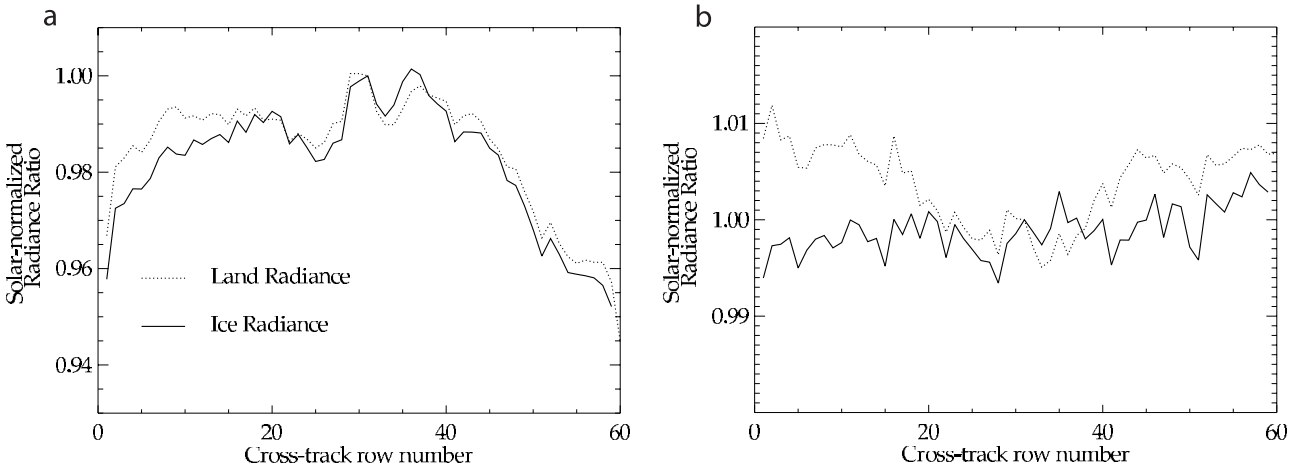

Figure 7. (a) A comparison of the error at 331 nm from ice radiances with the error derived over land surfaces as a function of row number for the collection 2 data. Both are normalized at row 31. The solid line is the ice radiance error, and the dotted line is the land radiance error. (b) Same as Figure 7a but for the collection 3 data. Note that the vertical scale is different than that of Figure 7a. The solid line is the ice radiance error, and the dotted line is the land radiance error.

the ice and land techniques. In both techniques this number is driven primarily by the uncertain knowledge of the bidirectional reflectance of the underlying surface.

[30] Figure 7 shows the collection 2 results for the ice radiance analysis and the land radiance analysis at 331 nm in the UV2 channel. It can be observed that, apart from small differences, the same structures and trends (up to 6%) as a function of row number are reproduced. The ice radiance analysis has been performed at all OMI wavelengths in the UV2 and VIS channels (310–504 nm), but cannot be trusted much shorter than 330 nm because of dependence of calculated radiances on column ozone amount. Little spectral dependence was observed in the derived radiance errors.

[31] A set of corrections derived from the ice radiance analysis is shown for the UV2 and VIS channels in Figure 8. These corrections have been applied to the prelaunch OPF radiance radiometric calibration data for collection 3. The difference between the UV2 and VIS corrections is consistent with interchannel differences observed in the prelaunch radiometric calibrations [*Dobber et al.*, 2006]. A comparable analysis of land radiances for the VIS channel has not been performed because of the technique's reliance on low surface reflectivity and large Rayleigh optical depth. Since the comparison between techniques shown in Figure 7 indicates the spatial fine structure is real rather than an analysis artifact, we have not smoothed the observed structure for either the UV2 or VIS channels. A set of corrections for the UV1 channel, also shown in Figure 8, is based entirely on UV2 results. At the time the collection 3 corrections were derived we had no independent validation of UV1 response. Subsequent comparisons with radiance predictions using ozone climatology suggest the UV1 swath dependence adjustment is nearly correct, but it should include some structure as in UV2 and VIS. The results for the ice and land radiance analyses after applying these corrections are shown in Figure 7. This plot is indicative of the residual errors found in the collection 3 data.

5. Earth Albedo

[32] The accuracy of trace gas retrievals and aerosol retrievals depends heavily on the quality of the surface albedo used. Several databases have been created using data from AVHRR [*Csiszar and Gutman*, 1999], TOMS [*Herman and Celarier*, 1997; *Herman et al.*, 2001] and GOME [*Koelemeijer et al.*, 2003], but these have limited spatial resolution or limited wavelength coverage. In order to provide accurate albedo maps for all retrievals using OMI data we set forth to create a database of ground reflectivities covering various wavelengths with a high spatial resolution of 0.5° by 0.5° and a temporal resolution of 1 month.

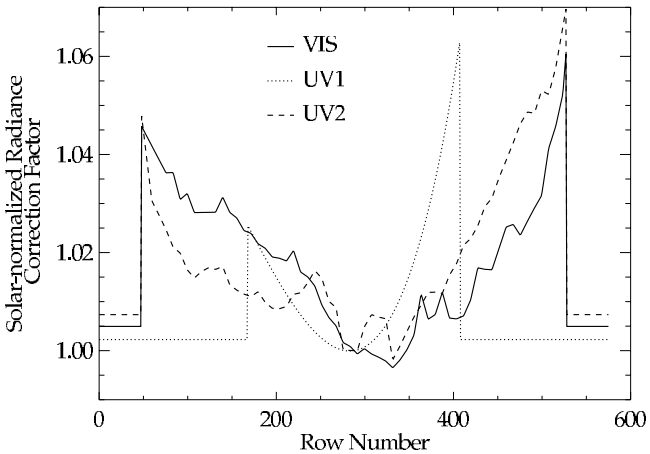

Figure 8. Final correction from ice radiances applied to detector rows for each channel. These corrections have been applied to the radiometric radiance calibration data in the OPF for collection 3.

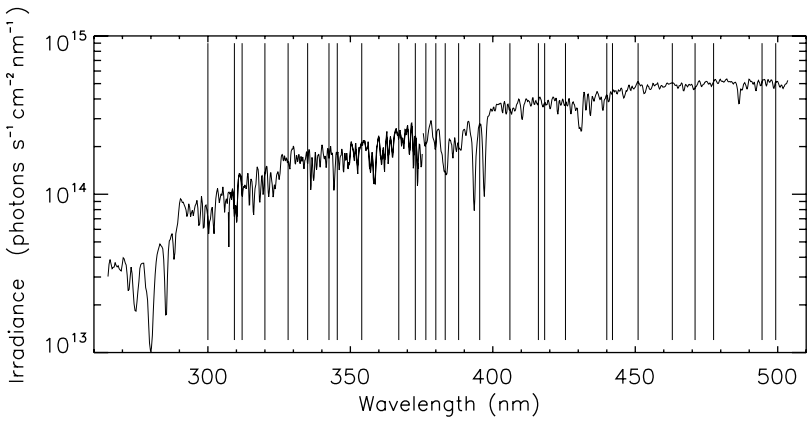

Figure 9. Target bands selected for calculation of the surface albedo plotted in the solar spectrum measured by OMI.

[33] A total of 35 target bands, shown in Figure 9, have been selected for various purposes. Some bands are used for aerosol and trace gas retrievals and some bands are chosen to coincide with earlier albedo studies using TOMS and GOME data. Bands with wavelengths in more than one channel (UV1, UV2, VIS) are extracted from both channels. These wavelength bands in the channel overlap ranges are used for validation of the reflectivities measured by OMI in the optical channels. Each band is approximately 1 nm wide. This is attained by averaging over several CCD detector pixels. This band width has been selected in order to simultaneously optimize the signal-to-noise and to minimize interference from the solar Fraunhofer structure. The spectral sampling in nm/pixel differs per channel, and so does the number of pixels that is averaged. The channel spacing in the UV1, UV2 and VIS channels is 0.32, 0.15 and 0.21 nm/pixel, respectively. Averaging over 3, 7 and 5 CCD pixels for the UV1, UV2 and VIS channels yields bandwidths of 0.96, 1.05 and 1.05 nm, respectively. For each level 1b radiance product measured by OMI all wavelength bands are extracted and divided by the corresponding irradiance product yielding the Sun-normalized Top Of the Atmosphere reflectance (TOA). The irradiance product used is measured on the same day as the radiance product to assure accurate correction for fluctuations in the measured solar spectrum originating from variations in the instrument response.

[34] The Lambert-Equivalent Reflectivity (LER) at a certain wavelength is found as the value of the surface albedo needed to match the measured reflectance at the top of the atmosphere assuming a clear sky atmosphere. Using a planar atmosphere radiative transfer model [*de Haan et al.*, 1987; *Stammes*, 2001], a lookup table has been created which describes the reflectivity at the top of the atmosphere as a function of the surface pressure, ozone column density, wavelength and measurement geometry. By interpolation in this lookup table the ground reflectivity can be found. Comparisons with a more accurate spherical atmosphere model show that the radiances calculated with the planar atmosphere radiative transfer model are accurate to approximately 1% for viewing zenith angles up to 70° for wavelengths larger than 320 nm. In order to create high-resolution surface albedo maps at different wavelengths, the LER data is regridded onto a 0.5° by 0.5° longitude/latitude grid. At this point the LER database still contains measurements contaminated by clouds and will thus yield surface albedo values that are too high. Using a histogram based method only the lowest measured value, that is called the Minimum Lambert-Equivalent Reflectivity (MLER), is selected. This MLER is taken to be equivalent to the surface albedo. The MLER is determined at one wavelength in the visible at 494.5 nm and the MLERs at the other wavelengths are determined from those ground scenes for which the MLER at 494.5 nm has this determined value. The wavelength of 494.5 nm has been used to maximize the contrast of the ground scenes.

[35] Figure 10 shows the annual MLER at 380 nm as determined from 3 years of OMI measurement data, along with the MLER differences with respect to the TOMS and GOME results. Figure 11 shows the histograms of the MLER differences between OMI and TOMS and between OMI and GOME. It can be observed that on average the OMI annual MLER at 380 nm is about one percent higher than the TOMS and GOME annual MLER. The absolute accuracy of the OMI MLER results is estimated to be about one percent also, depending somewhat on the ground scene, so the observed differences are just significant. The OMI histograms per ground scene at 380 nm in many cases do not show the low MLERs as reported for TOMS and for GOME, so it would appear that at 380 nm OMI indeed measures on average higher surface albedos than the other two instruments. The surface albedo results are derived by analyzing the histograms for TOMS at 380 nm, for GOME at 670 nm and for OMI at 494.5 nm. This difference can be part of the explanation why the observed OMI MLER values are slightly higher than the TOMS and GOME values. The differences will be further investigated in the future by comparing monthly MLERs and by making comparisons between OMI and GOME at other wavelengths.

[36] The OMI grid of 0.5° by 0.5° is not a limitation of the instrument. The GOME surface reflectivity database at 1.0° by 1.0° spatial resolution is based on 5.5 years of measurement data, the TOMS database at 1.0° by 1.25° even on 14.5 years of measurement data. The OMI results as shown in Figure 10 at a grid of 0.5° by 0.5° are based on only 3 years of measurement data. In order to collect

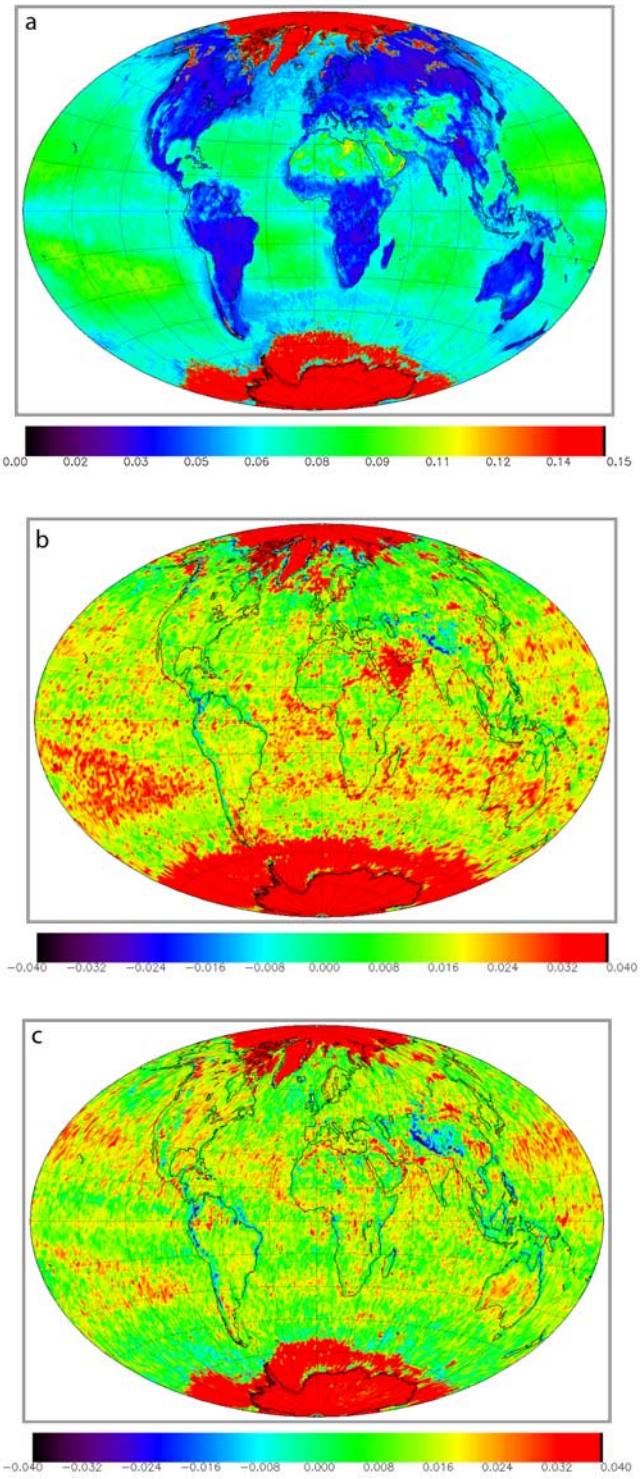

Figure 10. (a) Annual minimum LER values at 380 nm derived from 3 years of OMI measurements. (b) Annual minimum LER difference OMI − TOMS at 380 nm. (c) Annual minimum LER difference OMI − GOME at 380 nm.

sufficient data in the histograms for an accurate determination of the MLER we have limited the spatial resolution grid to 0.5° by 0.5°. When more measurement data becomes available we expect that we can reduce the grid to 0.1° by 0.1° in the future.

[37] As described above the Earth albedo is calculated in two optical channels for some wavelengths. This information can be used to validate the accuracy of the level 1b radiance data products in the channel overlap regions and to improve the instrument calibration in the future. Once accurate surface reflectivity values have been determined they can be used to validate the level 1b radiance product over time by looking at ground scenes for which the surface albedo is well known and constant over time. By observing such ground scenes at different viewing angles, we intend to validate the viewing angle dependence of the level 1b radiance in the future. Examples were shown in the previous section.

6. Stray Light

[38] The stray light correction algorithm is an important subtractive correction in the GDPS. The performance of the stray light correction algorithm in the collection 2 data has been extensively studied [*Dobber et al.*, 2006] and these investigations have identified a number of improvements that are discussed in this section. The stray light correction consists of two parts: the spatial stray light correction and the spectral stray light correction.

[39] The spatial stray light correction uses the signals from a number of dedicated stray light rows on the UV and VIS detectors above and below the directly illuminated regions on the detectors. The spatial stray light correction only depends on the viewing angles and does not couple source and target regions at different wavelengths. Spatial stray light is particularly important for ground scenes with high contrast, because the viewing directions with high signal levels may cause relatively high spatial stray light levels at viewing directions with low signal levels. All wavelengths in the upper and lower stray light rows are averaged and multiplied with predefined spectral shapes in the OPF. The OPF spectral shapes have been derived per instrument mode (radiance, irradiance, WLS) by investigating and averaging the signals in the dedicated stray light rows per instrument mode for many measurements. This analysis included both on-ground and in-flight measurement

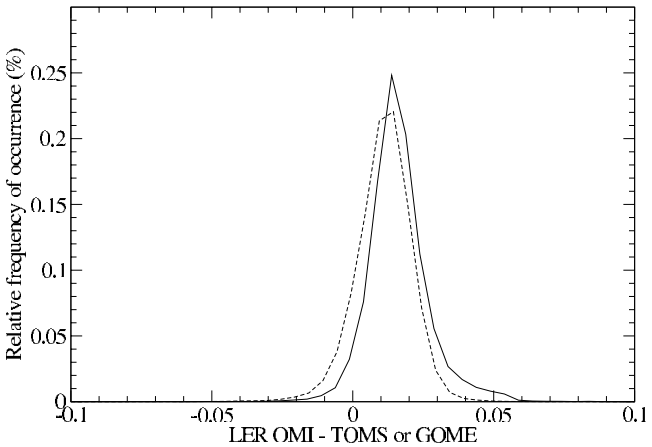

Figure 11. Histograms of the annual minimum LER difference OMI − TOMS at 380 nm (solid line) and of the annual minimum LER difference OMI − GOME at 380 nm (dashed line).

Table 1. Spatial and Spectral Stray Light Parameters for the Collection 2 and 3 Data Sets

	Collection 2			Collection 3		
Optical Channel	UV1	UV2	VIS	UV1	UV2	VIS
Spatial stray light correction	off	on	on	off	off	off
Spatial stray light row interpolation	no	no	no	linear	linear	linear
Spectral stray light rows source and target area	all	all	all	all	1	1

data. Subsequently a linear interpolation is performed between the upper and lower stray light rows to obtain the stray light at all rows. For the collection 2 data no spectral shape correction or linear interpolation is applied, but a simple average of the upper and lower stray light row signals at all wavelengths is used. A correction based on an average can significantly overestimate the stray light where signals are weak and underestimate where signals are strong. An overestimate occurs in the collection 2 data toward the long and short ends of each channel, where the signals are weaker. Significant errors occur for heterogeneous radiance scenes: basically an overcorrection for ground scenes with low light levels and an undercorrection for scenes with high light levels. Although this aspect has been corrected in the spatial stray light correction algorithm for the collection 3 data, the spatial stray light correction algorithm itself has been switched off for all channels for the collection 3 data set (see below).

[40] The second type of correction is the spectral stray light correction, which is particularly important for wavelength regions with low signal levels, e.g., below 300 nm or in the Fraunhofer lines. This correction is based on source (where the stray light is originating from) and target (where the stray light is going to) wavelength ranges, that can be located in different optical channels (UV1, UV2, VIS). The source term signal is multiplied with a predefined (in the OPF) polynomial shape as a function of wavelength in the target channel. The total amount of spectral stray light is composed of the sum of all such source/target combinations that have been identified in the prelaunch calibration. The remaining question concerns the spatial distribution of such a correction. In other words, how do stray photons from a specific spectral spatial source smear out spatially at the target wavelength? In the collection 2 data all rows in the illuminated image area in the source wavelength region are averaged and smeared out over all rows in the target optical channel. In the collection 3 data this has been changed so that the number of rows in the source and target areas can be set via OPF parameters per source/target combination. In this way the spectral stray light correction algorithm better corrects for spatial stray light as well. For this reason the spatial stray light correction (described above) has been switched off for all channels in the collection 3 data set in order to prevent an overcorrection of spatial stray light when the spectral and spatial stray light corrections are used simultaneously. Table 1 summarizes the stray light parameters described above for the collection 2 and 3 data.

[41] Stray light has been investigated using different methods. First, it is possible to investigate the signals in the UV1 optical channel below 290 nm as a function of time and correlate potentially observed structure with cloud features that appear at higher wavelengths, i.e., above 305 nm. Below 290 nm the ground and clouds are not visible, because nearly all light is scattered high in the Earth's atmosphere. Structures that are observed shorter than 290 nm are therefore most likely originating from imperfectly corrected spectral stray light. Figure 12 shows a representative example for the collection 3 data of signals at 280 nm in UV1 and above 305 nm in UV1 as function of orbit position for one orbit. The top curve shows the data at 280 nm that have not been corrected for stray light, the middle curve the data that have been optimally corrected for stray light. The middle curve has been normalized to the highest radiance near measurement number 800. The top curve has been normalized to this same corrected radiance and for this reason the values are higher than one. It can be observed that the spectral stray light contribution at 280 nm, where a strong solar Fraunhofer line is located and the useful signal is low, can be as high as 50%. At other wavelengths the relative spectral stray light fraction is much smaller. The bottom curve shows the radiances at the longer wavelengths, normalized to its highest value and scaled arbitrarily by 0.6 in order to introduce an offset in the plot for clarity. The clouds can be seen clearly as peaks at the longer wavelengths (bottom curve) and in the uncorrected data at 280 nm (top curve), whereas in the stray light corrected data at 280 nm no distinct and corresponding structures are visible (middle curve), indicating that the spectral stray light has been properly corrected. Also note the correlation in the cloud structures between the top and bottom curves in Figure 12.

[42] Another way of investigating stray light is to look at the channel overlap regions UV1/UV2 around 307–311 nm and UV2/VIS around 349–383 nm. The radiances in both channels should be the same, if all calibrations are accurate.

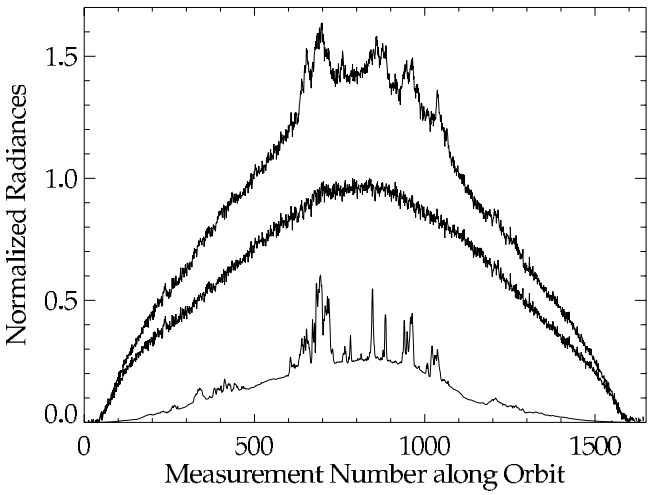

Figure 12. OMI measurement data in the UV1 channel at 280 nm that have not been corrected for spectral stray light (top curve) and data that have been corrected for spectral stray light (middle curve) for the collection 3 data. The bottom curve shows the radiances at the higher wavelengths (above 305 nm), multiplied by 0.6 in order to introduce an offset in the plot for clarity.

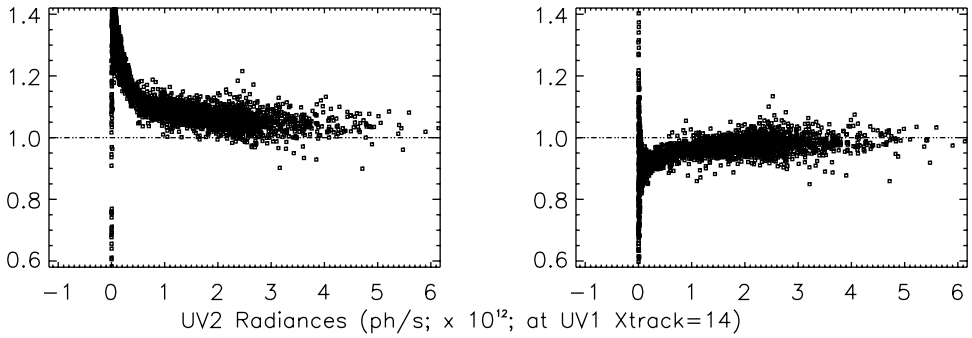

Figure 13. UV1/UV2 radiance ratios as function of radiance level in the UV2 channel at the nadir viewing position at 310.1 nm (left) for collection 2 data and (right) for collection 3 data.

The weaker signals in these regions make them more sensitive to stray light errors. Figures 13 and 14 show two of many examples for the UV1/UV2 overlap region at 310.1 nm and the UV2/VIS overlap region at 354.8 nm for collection 2 and collection 3 data. SO_2 retrievals at 310 nm in the UV1/UV2 channel overlap and aerosol retrievals that use the 354 nm band in the VIS channel are particularly sensitive to errors in the stray light correction, because the useful signals are low at these wavelengths. Figures 13 and 14 show the ratio of the radiances measured in the two channels as a function of the signal level in one of the channels. Ratios that change as a function of signal level are indications of additive errors, such as stray light, whereas signal-independent offsets are indications of multiplicative errors, such as the radiometric correction. Figures 13 and 14 show that multiplicative errors of up to about 5% in the collection 2 data have been removed in the collection 3 data. Figure 13 also shows inconsistencies in the additive correction factors (stray light) in the UV1 and UV2 channels of up to 40% for the collection 2 data and an improvement to inconsistencies of about 10% for the collection 3 data in the UV1/UV2 channel overlap. Figure 14 shows inconsistencies of about 3% for the collection 2 data and an improvement to consistent behavior in the collection 3 data in the UV2/VIS channel overlap. The exact quantitative numbers vary with viewing direction and wavelength. The impact of the stray light correction algorithm changes from collection 2 to 3 is negligible for the UV1 channel and for the wavelength regions in the UV2 and VIS channels that are not in the UV1/UV2 (307–311 nm) or UV2/VIS (349–383 nm) channel overlap regions.

[43] Analysis of the collection 2 data with the methods described above reveals that too much stray light is subtracted in the UV2 and VIS channels. This is most likely due to the fact that both the spatial and the spectral stray light corrections are switched on simultaneously for these channels, whereas the spectral stray light correction coefficients were derived from on-ground measurement data with the spatial stray light correction algorithm switched off. Since the row-averaging in the spectral stray light correction algorithm also corrects to some extent for spatial stray light, using both stray light correction algorithms simultaneously overcorrects the total stray light. For this reason the spatial stray light correction has been switched off for all channels for the collection 3 data. Note that it was already switched off in the UV1 channel (Table 1) for the collection 2 data. The results discussed in this section for the collection 3 data show that this approach leads to a more consistent stray light correction at all wavelengths than in the collection 2 data.

7. Conclusions and Future Work

[44] The validation of the collection 2 level 1b radiance and irradiance data measured by the OMI instrument on board of NASA's EOS-Aura satellite has been discussed in detail, along with a number of improvements that have been made from collection 2 to collection 3 data. With these improvements in the OPF and in the GDPS the accuracy of the level 1b radiance and irradiance in collection 3 is improved.

[45] A new high-resolution irradiance reference spectrum with high spectral sampling and good radiometric calibration

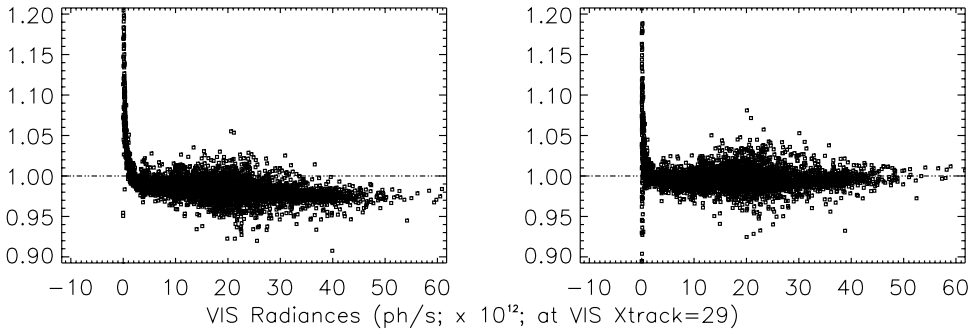

Figure 14. UV2/VIS radiance ratios as function of radiance level in the VIS channel at the nadir viewing position at 354.8 nm (left) for collection 2 data and (right) for collection 3 data.

has been derived for the wavelength range 250–550 nm. The OMI level 1b irradiance from the collection 3 data agrees with the newly derived high-resolution reference irradiance spectrum to within 3% for high-frequency structures correlated with the solar Fraunhofer lines, to within 0.5% for lower-frequency features and also to within 4% with other irradiance spectra from the literature. The in-orbit wavelength-dependent radiometric degradation is smaller than 0.5% above 310 nm and increases to about 1.2% at 270 nm after 2.5 years. On average, the OMI surface albedo values at 380 nm, that have absolute accuracies of about one percent, are higher by about one percent than the albedos as observed with the TOMS and GOME instruments at the same wavelength.

[46] Using the improved collection 3 level 1b data we intend to further improve the viewing angle dependence of the radiance and the spectral stray light correction. We will continue to monitor potential instrumental degradation and correct for this if necessary. We will continue and expand the surface albedo analyses in the future with the purpose to deliver surface albedo maps with a monthly time resolution at a number of wavelengths in the range 310–500 nm. These albedo maps can be used to improve other retrievals, that make use of OMI measurement data. In addition, the surface albedo will be used to further validate the level 1b radiance.

References

Chance, K. V., and R. J. D. Spurr (1997), Ring effect studies: Rayleigh scattering, including molecular parameters for rotational Raman scattering, and the Fraunhofer spectrum, *Appl. Opt.*, *36*, 5224–5230.

Csiszar, I., and G. Gutman (1999), Mapping global land surface albedo from NOAA AVHRR, *J. Geophys. Res.*, *104*, 6215–6228, doi:10.1029/1998JD200090.

de Haan, J. F., P. B. Bosma, and J. W. Hovenier (1987), The adding method for multiple scattering calculations of polarized light, *Astron. Astrophys.*, *183*, 371–391.

Dirksen, R., M. Dobber, R. Voors, and P. Levelt (2006), Prelaunch characterization of the Ozone Monitoring Instrument transfer function in the spectral domain, *Appl. Opt.*, *45*(17), 3972–3981, doi:10.1364/AO.45.003972.

Dobber, M. R., et al. (2006), Ozone Monitoring Instrument calibration, *IEEE Trans. Geosci. Remote Sens.*, *44*(5), 1209–1238, doi:10.1109/TGRS.2006.869987.

Dobber, M. R., R. Voors, R. Dirksen, Q. Kleipool, and P. Levelt (2008), The high-resolution solar reference spectrum between 250 and 550 nm and its application to measurements with the Ozone Monitoring Instrument, *Sol. Phys.*, in press.

Floyd, L., G. Rottman, M. DeLand, and J. Pap (2003), in Proc. ISCS 2003 Symposium "Solar Variability as an input to the Earth's Environment", ESA SP-535.

Gurlit, W., et al. (2005), The UV-A and visible solar irradiance spectrum: Inter-comparison of absolutely calibrated, spectrally medium resolution solar irradiance spectra from balloon- and satellite-borne measurements, *Atmos. Chem. Phys.*, *5*, 1879–1890.

Hall, L. A., and G. P. Anderson (1991), High-resolution solar spectrum between 2000 and 3100 Å, *J. Geophys. Res.*, *96*, 12,927–12,931, doi:10.1029/91JD01111.

Herman, J. R., and E. A. Celarier (1997), Earth surface reflectivity climatology at 340–380 nm from TOMS data, *J. Geophys. Res.*, *102*(D23), 28,003–28,011, doi:10.1029/97JD02074.

Herman, J. R., E. Celarier, and D. Larko (2001), UV 380 nm reflectivity of the Earth's surface, clouds and aerosols, *J. Geophys. Res.*, *106*(D6), 5335–5351, doi:10.1029/2000JD900584.

Jaross, G., and J. Warner (2008), Use of Antarctica for validating reflected solar radiation measured by satellite sensors, *J. Geophys. Res.*, doi:10.1029/2007JD008835, in press.

Koelemeijer, R. B. A., J. F. de Haan, and P. Stammes (2003), A database of spectral surface reflectivity in the range 335–772 nm derived from 5.5 years of GOME observations, *J. Geophys. Res.*, *108*(D2), 4070, doi:10.1029/2002JD002429.

Kurucz, R. L., I. Furenlid, J. Brault, and L. Testerman (1984), Solar flux atlas from 296 to 1300 nm, Natl. Sol. Obs., Sunspot, N. M. (Available at ftp://ftp.noao.edu/fts/fluxatl)

Levelt, P. F., E. Hilsenrath, G. W. Leppelmeier, G. H. J. van den Oord, P. K. Bhartia, J. Tamminen, J. F. de Haan, and J. P. Veefkind (2006), Science objectives of the Ozone Monitoring Instrument, *IEEE Trans. Geosci. Remote Sens.*, *44*(5), 1199–1208, doi:10.1109/TGRS.2006.872336.

Stammes, P. (2001), Spectral radiance modeling in the UV-visible range, in *IRS200: Current Problems in Atmospheric Radiation*, edited by W. L. Smith and Y. M. Timofeyev, pp. 385–388, A. Deepak, Hampton, Va.

Thuillier, G., M. Hersé, D. Labs, T. Foujols, W. Peetermans, D. Gillotay, P. C. Simon, and H. Mandel (2003), The solar spectral irradiance from 200 to 2400 nm as measured by the SOLSPEC spectrometer from the ATLAS and EURECA missions, *Sol. Phys.*, *214*, 1–22, doi:10.1023/A:1024048429145.

Thuillier, G., L. Floyd, T. N. Woods, R. Cebula, E. Hilsenrath, M. Hersé, and D. Labs (2004), Solar irradiance reference spectra for two solar active levels, *Adv. Space Res.*, *34*, 256–261, doi:10.1016/j.asr.2002.12.004.

van den Oord, G. H. J., J. P. Veefkind, P. F. Levelt, and M. R. Dobber (2006), OMI Level 0 to 1b processing and operational aspects, *IEEE Trans. Geosci. Remote Sens.*, *44*(5), 1380–1397, doi:10.1109/TGRS.2006.872935.

R. Dirksen, M. Dobber, Q. Kleipool, P. Levelt, and N. Rozemeijer, Royal Netherlands Meteorological Institute, P.O. Box 201, NL-3730 AE De Bilt, Netherlands.

L. Flynn, NOAA, 5200 Auth Road, Camp Springs, MD 20746, USA.

G. Jaross, T. Kelly, and S. Taylor, Science Systems and Applications Inc., Greenbelt, MD 20706, USA.

G. Leppelmeier, G & S Associates, Yläkaupinkuja 2, FIN-02360, Espoo, Finland.